8-2023

Self-Calibrating Optical Galaxy Cluster Selection Bias Using Cluster, Galaxy, and Shear Cross-Correlations

Chenxiao Zeng
Ohio State University

Andrés N. Salcedo
University of Arizona

Hao-Yi Wu
Boise State University

Christopher M. Hirata
Ohio State University

https://doi.org/10.1093/mnras/stad1649

Monthly Notices of the ROYAL ASTRONOMICAL SOCIETY

MNRAS **523,** 4270–4281 (2023) https://doi.org/10.1093/mnras/stad1649
Advance Access publication 2023 June 05

Self-calibrating optical galaxy cluster selection bias using cluster, galaxy, and shear cross-correlations

Chenxiao Zeng [1,2★] Andrés N. Salcedo [3★] Hao-Yi Wu [4★] and Christopher M. Hirata [1,2,5★]

[1] *Department of Physics, The Ohio State University, 191 West Woodruff Avenue, Columbus, OH 43210, USA*
[2] *Center for Cosmology and AstroParticle Physics, The Ohio State University, Columbus, OH 43210, USA*
[3] *Department of Astronomy/Steward Observatory, University of Arizona, 933 North Cherry Avenue, Tucson, AZ 85721-0065, USA*
[4] *Department of Physics, Boise State University, Boise, ID 83725, USA*
[5] *Department of Astronomy, The Ohio State University, 140 West 18th Avenue, Columbus, OH 43210, USA*

Accepted 2023 May 26. Received 2023 May 2; in original form 2022 October 28

ABSTRACT

The clustering signals of galaxy clusters are powerful tools for self-calibrating the mass–observable relation and are complementary to cluster abundance and lensing. In this work, we explore the possibility of combining three correlation functions – cluster lensing, the cluster–galaxy cross-correlation function, and the galaxy autocorrelation function – to self-calibrate optical cluster selection bias, the boosted clustering and lensing signals in a richness-selected sample mainly caused by projection effects. We develop mock catalogues of redMaGiC-like galaxies and redMaPPer-like clusters by applying halo occupation distribution models to *N*-body simulations and using counts-in-cylinders around massive haloes as a richness proxy. In addition to the previously known small-scale boost in projected correlation functions, we find that the projection effects also significantly boost three-dimensional correlation functions to scales of 100 h^{-1} Mpc. We perform a likelihood analysis assuming survey conditions similar to the Dark Energy Survey and show that the selection bias can be self-consistently constrained at the 10 per cent level. We discuss strategies for applying this approach to real data. We expect that expanding the analysis to smaller scales and using deeper lensing data would further improve the constraints on cluster selection bias.

Key words: gravitational lensing: weak – galaxies: clusters: general – cosmology: theory.

1 INTRODUCTION

The abundance of galaxy clusters across cosmic time reflects the growth rate of cosmic structure and is a sensitive probe of cosmic acceleration (see e.g. Frieman, Turner & Huterer 2008; Allen, Evrard & Mantz 2011; Weinberg et al. 2013; Huterer et al. 2015). The halo mass function predicts the halo number density as a function of mass and redshift for a given set of cosmological parameters (see e.g. Press & Schechter 1974; Sheth, Mo & Tormen 2001; Tinker et al. 2008). To connect this theoretical prediction with the observed cluster abundance, we need well-calibrated and unbiased mass–observable relations. The mass–observable relation can be derived from combinations of X-ray luminosity and temperature (e.g. Rozo & Rykoff 2014; Giles et al. 2022), Sunyaev–Zeldovich (SZ) effect (e.g. Saro et al. 2015; Bleem et al. 2020), galaxy velocity dispersion (e.g. Bocquet et al. 2015; Rozo et al. 2015), and weak gravitational lensing (e.g. Melchior et al. 2017; Simet et al. 2017; Murata et al. 2018, 2019; Dietrich et al. 2019; McClintock et al. 2019). The accuracy of the mass–observable relation critically impacts the constraining power of the cluster sample (e.g. Wu et al. 2021).

Deriving cosmological parameter constraints by combining observed cluster abundances and the mass–observable relation has been the strategy of many previous studies (e.g. Vikhlinin et al. 2009; Mantz et al. 2010, 2014; Rozo et al. 2010; Bocquet et al. 2015, 2019; de Haan et al. 2016; Planck Collaboration XIII 2016; Abbott et al. 2020; Costanzi et al. 2021). A complementary approach would be to use the clustering of clusters (correlation functions or power spectra) to self-calibrate the mass–observable relation (e.g. Lima & Hu 2004, 2005; Majumdar & Mohr 2004; Wu, Rozo & Wechsler 2008; Salcedo et al. 2020). This strategy has been applied to X-ray surveys (e.g. Collins et al. 2000; Schuecker et al. 2003; Balaguera-Antolínez et al. 2011) and optical surveys (e.g. Croft, Dalton & Efstathiou 1999; Sánchez et al. 2005; Estrada, Sefusatti & Frieman 2009; Mana et al. 2013; Baxter et al. 2016; Paech et al. 2017; Chiu et al. 2020; To et al. 2021; Park et al. 2023). In particular, recent wide-field optical surveys have enabled precision cosmology analyses using cluster clustering. For example, To et al. (2021) combine the autocorrelation and cross-correlation between clusters, galaxies, and shear from the Dark Energy Survey (DES) to derive competitive cosmological constraints.

However, recent studies show that optically selected galaxy clusters exhibit selection bias in their lensing and clustering signals (Abbott et al. 2020; Sunayama et al. 2020; Wu et al. 2022). In particular, at a given mass, a richness-selected sample tends to have a higher lensing and clustering signal than expected from its mass. This selection bias, if not accounted for, will lead to biased cluster mass calibration and cosmological parameters. This selection bias has been mostly ignored in previous studies but has become one of

★ E-mail: zeng.544@osu.edu (CZ); ansalcedo@arizona.edu (ANS); hywu@boisestate.edu (HYW); hirata.10@osu.edu (CMH)

Table 1. Fiducial values and descriptions for HOD parameters for the mock redMaGiC galaxy catalogues.

Parameter	Fiducial	Description
$\sigma_{\log M}$	0.60	Width of central transition
$\log M_{\rm min}$	12.7	Minimum halo mass to host a central
$\log M_0$	11.0	Satellite cut-off mass
$\log M_1$	13.8	Minimum halo mass to host a satellite
α	1.50	Slope of satellite occupation power law
$f_{\rm cen}$	0.60	Central completeness fraction

Table 2. Similar to Table 1, but for galaxies that match the colour–magnitude selection of the member galaxies of redMaPPer clusters. This HOD is different from that for redMaGiC galaxies because they correspond to different selection criteria.

Parameter	Fiducial	Description
$\log M_{\rm min}$	12	Mass threshold of haloes
$\log M_0$	11.7	Same as in Table 1
$\log M_1$	12.9	Same as in Table 1
α	1	Same as in Table 1

the dominant systematic uncertainties for current DES data (Abbott et al. 2020).

In this work, we use multiple correlation functions to self-calibrate optical cluster selection bias. Salcedo et al. (2020) have previously shown that combining cluster lensing, cluster–galaxy cross-correlations, and galaxy autocorrelations provides an effective way to break the degeneracy between the scatter in the richness–mass relation and the matter density fluctuation amplitude σ_8. The basic idea is that these three observables can be combined to solve for three unknowns: cluster bias $b_{\rm c}$, galaxy bias $b_{\rm g}$, and σ_8. The resulting $b_{\rm c}$ directly constrains the scatter. We similarly use these observables to simultaneously solve for $b_{\rm g}$, $b_{\rm c}$, and σ_8; here, $b_{\rm c}$ includes the effect of selection bias. We construct mock cluster and galaxy samples by applying the halo occupation distribution (HOD) framework (e.g. Berlind & Weinberg 2002; Cooray & Sheth 2002; Zheng et al. 2005; Zehavi et al. 2011) to the ABACUS COSMOS N-body simulation suite. We calculate three-dimensional (3D) and two-dimensional (2D) correlation functions between clusters, galaxies, and matter. We show that we can correctly recover the cluster bias $b_{\rm c}$ and σ_8 by fitting these correlation functions simultaneously. We focus on scales greater than 10 h^{-1} Mpc and defer small-scale calibration to future work. This work paves the way for an analysis using wide-field survey data like DES and Vera C. Rubin Observatory's Legacy Survey of Space and Time (LSST).

This paper is organized as follows. Section 2 describes the simulated mock catalogues, and Section 3 describes our measurements of correlation functions. In Section 4, we present the likelihood analysis for self-calibrating cluster selection bias and constraining cosmological parameters. We discuss our results in Section 5 and summarize in Section 6. In this work, we use the fiducial flat *Planck* Lambda cold dark matter cosmology (Planck Collaboration XIII 2016) adopted by the ABACUS COSMOS simulation suite: $\Omega_{\rm M} = 0.314$, $h = 0.673$, $\sigma_8 = 0.83$, $n_{\rm s} = 0.9652$, and $\Omega_{\rm B} = 0.049$. All distances are in comoving h^{-1} Mpc. We use the spherical overdensity mass definition $M_{\rm 200m}$, defined such that the mean density enclosed is 200 times the mean density of the Universe.

2 MOCK GALAXY AND CLUSTER CATALOGUES

We generate mock galaxy catalogues by applying HOD models to the ABACUS COSMOS N-body simulations. We apply two sets of HOD parameters. The first one simulates redMaGiC galaxies, which have precise photometric redshifts and are optimized for calculating cross-correlation and autocorrelation functions (Table 1). The second one simulates the members of redMaPPer clusters (Table 2). Below, we describe our approach in detail.

2.1 ABACUS COSMOS N-body simulations

We build our mock galaxy and cluster catalogues using the public ABACUS COSMOS N-body simulation suite[1] (Garrison et al. 2018), which is based on the ABACUS N-body code (Metchnik 2009; Garrison et al. 2018). We use 20 periodic boxes of the fiducial *Planck* cosmology with varied phases in the initial conditions, with a box size 1100 h^{-1} Mpc (internally called $AbacusCosmos\_1100box\_planck$). We focus on the $z = 0.3$ outputs in this work. Each simulation box contains 1440^3 dark matter particles, corresponding to a mass resolution of $4 \times 10^{10}\, h^{-1}\, {\rm M}_\odot$, and has a spline softening of 63 h^{-1} kpc. Dark matter halo catalogues are created by applying the ROCKSTAR halo finder (Behroozi, Wechsler & Wu 2013) to particle snapshots. For assigning galaxies to haloes, we use host haloes defined by ROCKSTAR and the mass definition $M_{\rm 200m}$. For the lensing calculations, we use a 0.1 per cent subsample of the dark matter particles, and we have tested that this downsampling can accurately recover the lensing signal well below 0.1 h^{-1} Mpc.

2.2 Mock redMaGiC sample

The redMaGiC (red-sequence Matched-filter Galaxy Catalog) galaxy samples (Rozo et al. 2016) are designed to minimize photometric redshift uncertainties and have been used in various galaxy clustering and lensing studies (e.g. Abbott et al. 2018). We populate simulated ABACUS COSMOS haloes with mock DES redMaGiC galaxies using an HOD model. As in Salcedo et al. (2022), we extend this framework to include central incompleteness, which is known to affect redMaGiC galaxies due to the strict colour selection criteria. We parametrize the mean central and satellite occupations of our haloes as

$$\langle N_{\rm cen}|M_{\rm h}\rangle = \frac{f_{\rm cen}}{2}\left[1 + {\rm erf}\left(\frac{\log M_{\rm h} - \log M_{\rm min}}{\sigma_{\log M}}\right)\right], \quad (1)$$

$$\langle N_{\rm sat}|M_{\rm h}\rangle = \frac{\langle N_{\rm cen}|M_{\rm h}\rangle}{f_{\rm cen}}\left(\frac{M_{\rm h} - M_0}{M_1}\right)^{\alpha}, \quad (2)$$

where $f_{\rm cen}$ allows for central incompleteness, i.e. the fact that not all high-mass haloes have a central satisfying the redMaGiC selection criteria. Table 1 lists the fiducial values we assume for each of our parameters.

The number of mock central and satellite galaxies placed into each halo is drawn randomly from a binomial and Poisson distribution, respectively, with mean occupations as given above. Centrals are placed at the centre of their host halo, while satellites are distributed according to a Navarro–Frenk–White profile (Navarro, Frenk & White 1997) parametrized by halo concentration $c_{\rm 200m}$ assigned using the fits of Correa et al. (2015). The extent to which satellite galaxies trace their host halo's dark matter profile is an open question, but because our analysis only relies on large scales ($r > 10\, h^{-1}$ Mpc)

[1] https://lgarrison.github.io/AbacusCosmos/

our results are unaffected by the assumption that galaxy and halo concentrations are the same.

2.3 Mock redMaPPer sample

The redMaPPer (red-sequence Matched-filter Probabilistic Percolation) cluster-finding algorithm (Rykoff et al. 2014, 2016) identifies clusters from multiband photometric galaxy catalogues by searching for overdense regions of red galaxies. The algorithm first trains the red sequence – the tight relation between colour and magnitude for galaxies in clusters – as a function of redshift. The algorithm then uses this red-sequence model to calculate the probability that a galaxy is a member of a potential cluster centre. The sum of the membership probabilities is the richness of a cluster.

At the beginning of the iteration, all red galaxies are considered potential cluster centres. After each iteration, potential cluster centres are ranked by their richness values. A galaxy near multiple cluster centres has a higher priority to be counted towards a higher ranked centre (a process called 'percolation'). The algorithm iterates this process until the resulting cluster catalogue converges.

In principle, one could apply the redMaPPer algorithm to a mock galaxy catalogue; for example, it has been applied to the Buzzard simulations (DeRose et al. 2019) and the CosmoDC2 simulation (Kovacs et al. 2022). However, such a calculation is expensive and requires us to simulate accurate galaxy colours. Therefore, in this work, we simulate the redMaPPer catalogue using a simplified counts-in-cylinders approach introduced by Costanzi et al. (2019) and Sunayama et al. (2020).

In the first step of our mock redMaPPer algorithm, we simulate the 'parent population' of redMaPPer member galaxies – galaxies with colours consistent with the redMaPPer clusters' red sequence and have the potential to be identified as cluster members. This step is similar to the initial colour and magnitude selection of the redMaPPer algorithm. These galaxies can contribute to cluster members if they are near the line of sight of a massive halo.

We adopt the HOD parametrization in Sunayama et al. (2020) for this parent population. We assign a central to each halo above $M_{\rm min} = 10^{12}\,h^{-1}\,{\rm M}_\odot$. For satellite galaxies, we assume

$$\langle N_{\rm sat}|M_{\rm h}\rangle = \langle N_{\rm cen}|M_{\rm h}\rangle \left(\frac{M_{\rm h}-M_0}{M_1}\right)^{\alpha}, \quad (3)$$

and we list the fiducial values in Table 2. We emphasize that the HOD model for the redMaPPer parent population is different from that of the redMaGiC galaxies introduced earlier. Although redMaGiC galaxies and redMaPPer member galaxies are both red, they have different colour and magnitude selection criteria and thus different HODs.

In the second step, we mimic the redMaPPer cluster-finding procedure by counting galaxies within a cylinder along the line of sight. We use a cylinder depth of $\pm 30\,h^{-1}$ Mpc (comoving distance along the line of sight). In Wu et al. (2022), we have shown that this projection depth well describes the projection effects and selection bias of redMaPPer in the Buzzard simulations.

We assume that each galaxy can only be a member of a single cluster; that is, when a galaxy falls in the cylinders of multiple haloes, it is counted as a member of the most massive one. This simulates the percolation process of redMaPPer. The resulting number of galaxies inside a cylinder is our mock richness λ. The aperture of the cylinder

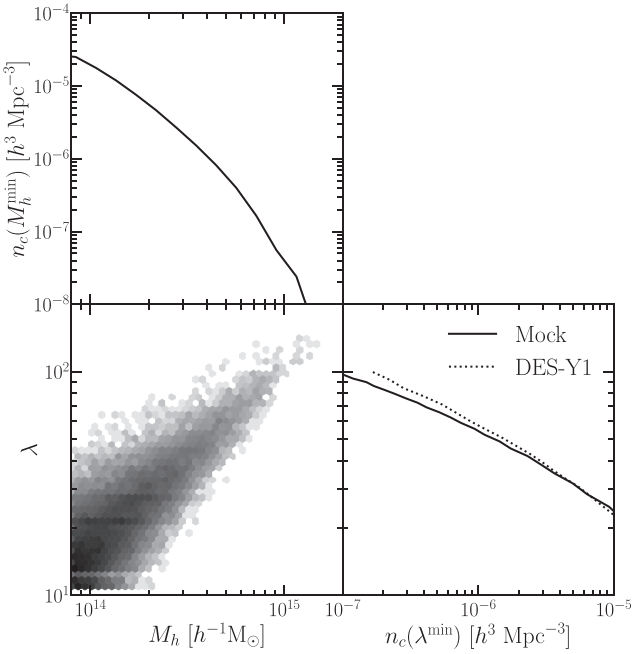

Figure 1. Richness–mass relation for one of our mock cluster catalogues based on HOD and counts-in-cylinder cluster finding. The top and right-hand panels show the cumulative number density above a given mass and richness, respectively. The cluster abundances from our mock catalogues are broadly consistent with those from DES Y1 cluster sample (Y1CL), shown as the dotted curve in the right-hand panel.

is calculated iteratively based on λ:

$$R_\lambda = \left(\frac{\lambda}{100}\right)^{0.2} \quad \text{physical } h^{-1}\,\text{Mpc}. \quad (4)$$

Fig. 1 presents the richness–mass relation of one of our mock redMaPPer catalogues (phase 0). The hexagonal binning presents the number density of haloes in each richness–mass cell. We show the cumulative number density as a function of the mass threshold (top panel) and the richness threshold (right-hand panel). In the right-hand panel, we add the cumulative cluster number density versus richness from the DES Y1 redMaPPer catalogue[2] (Abbott et al. 2020, hereafter Y1CL). The catalogue covers 1437 deg^2, and we focus on clusters in the redshift range $0.2 < z < 0.35$. We assume $\Omega_{\rm M} = 0.3$ when converting cluster counts to comoving density in the unit of comoving $h^3\,{\rm Mpc}^{-3}$. As can be seen, our mock cluster catalogue has a cluster abundance similar to that of the DES Y1 redMaPPer catalogue.

For the correlation function calculations, we define a mass-selected halo sample and a richness-selected cluster sample. For the former, we focus on haloes with $M_{\rm 200m} \geq 2 \times 10^{14}\,h^{-1}\,{\rm M}_\odot$. This threshold corresponds to approximately 7500 haloes per simulation box of $1100\,h^{-1}$ Mpc and a number density $\approx 5.8 \times 10^{-6}\,h^3\,{\rm Mpc}^{-3}$, which corresponds to a richness $\lambda \approx 30$ in Y1CL. We then define a richness-selected sample by abundance matching; that is, we sort clusters by their richness values and select the top N clusters that match this number density.

[2]The DES Y1 redMaPPer catalogue is publicly available at https://des.ncsa.illinois.edu.

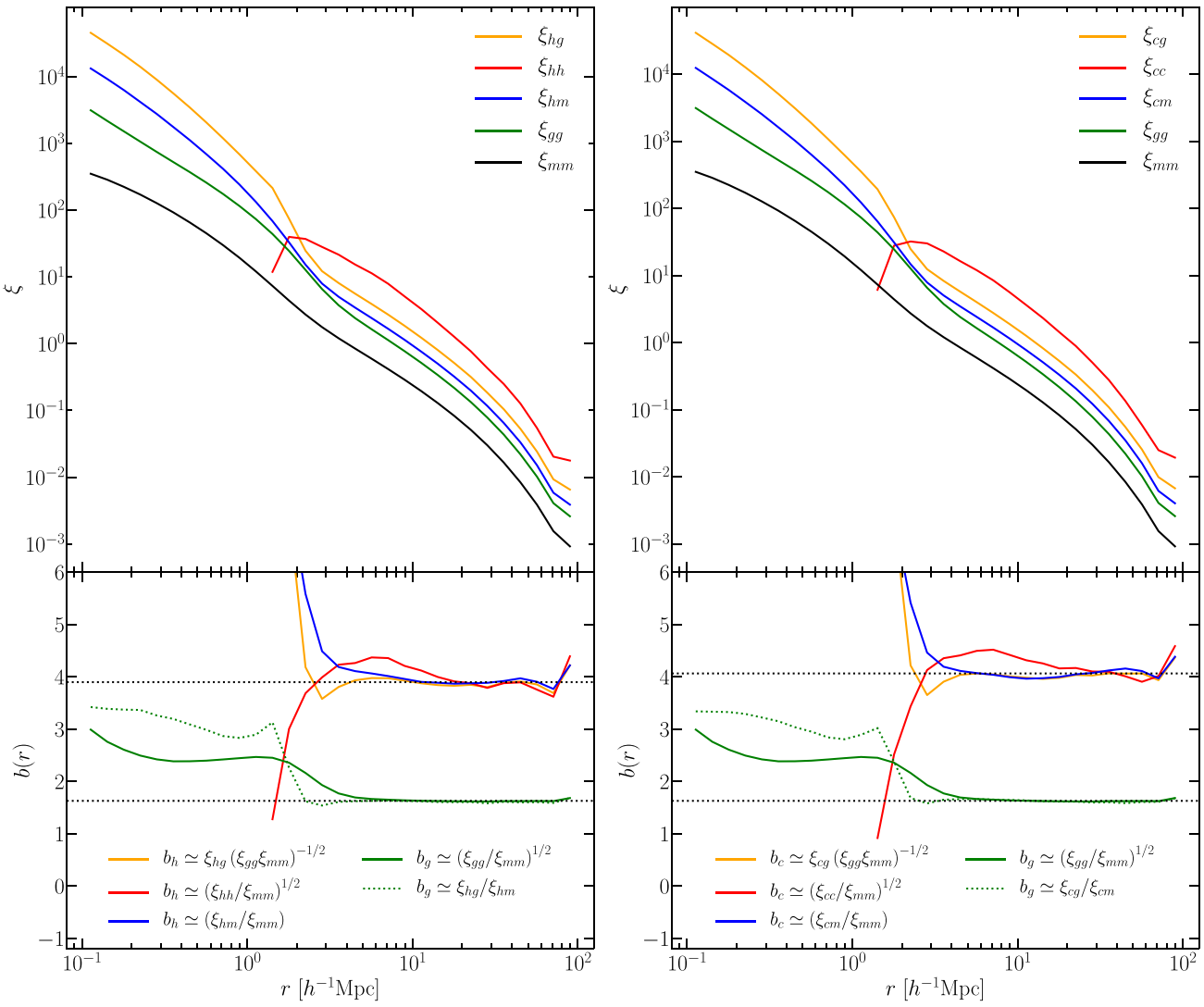

Figure 2. Top: 3D two-point correlation functions $\xi(r)$ for different pairs of objects, calculated by averaging over 20 mock catalogues. Bottom: halo/cluster bias and galaxy bias solved by combining various correlation functions. Left: haloes above $2 \times 10^{14}\ h^{-1}\,\mathrm{M}_{\odot}$. The average halo bias b_{h} and galaxy bias b_{g} at scales larger than $10\ h^{-1}$ Mpc are 3.89 and 1.62, respectively, shown as the horizontal dotted lines. Right: richness-selected clusters with the same number density as the left-hand panel. The average cluster bias b_{c} and b_{g} at scales larger than $10\ h^{-1}$ Mpc are 4.06 and 1.63, respectively.

3 CLUSTER CORRELATION FUNCTION OBSERVABLES

With the mock cluster and galaxy catalogues, we are ready to calculate various two-point correlation functions. Below, we briefly introduce the basics of two-point correlation functions and describe our measurements.

3.1 Basics for correlation functions

The two-point cross-correlation function between two sets of points A and B, $\xi_{\mathrm{AB}}(r)$, is defined in terms of the joint probability δP of finding objects in two volume elements $(\delta V_{\mathrm{A}},\ \delta V_{\mathrm{B}})$ separated by some distance r,

$$\delta P = n_{\mathrm{A}} n_{\mathrm{B}} \delta V_{\mathrm{A}} \delta V_{\mathrm{B}}\,[1 + \xi_{\mathrm{AB}}(r)]\,, \tag{5}$$

where n_{A} and n_{B} are the respective number densities of sets A and B (Peebles 1980). The correlation function represents the excess in spatial clustering of sets A and B relative to two uncorrelated sets of points. Since we use periodic simulation boxes, the correlation functions can be accurately obtained by the natural estimator:

$$\xi_{\mathrm{AB}}(r) = \frac{\mathrm{AB}(r)}{\mathrm{RR}(r)} - 1, \tag{6}$$

where $\mathrm{AB}(r)$ is the number of A–B pairs with separation r, and $\mathrm{RR}(r)$ is the expected number of pairs in random samples with the same respective number densities and volume geometry. We calculate the $RR(r)$ analytically using the number densities of A and B.

We first calculate the 3D galaxy autocorrelation function ξ_{gg}, cluster–galaxy cross-correlation function ξ_{cg}, and cluster–matter cross-correlation function ξ_{cm}. We use the CORRFUNC software package (Sinha & Garrison 2017) with 30 logarithmically spaced bins r between 0.1 and 100 h^{-1} Mpc. Fig. 2 shows our measurements of various $\xi(r)$ functions averaged over 20 mock catalogues.

The projected correlation function is related to the 3D correlation

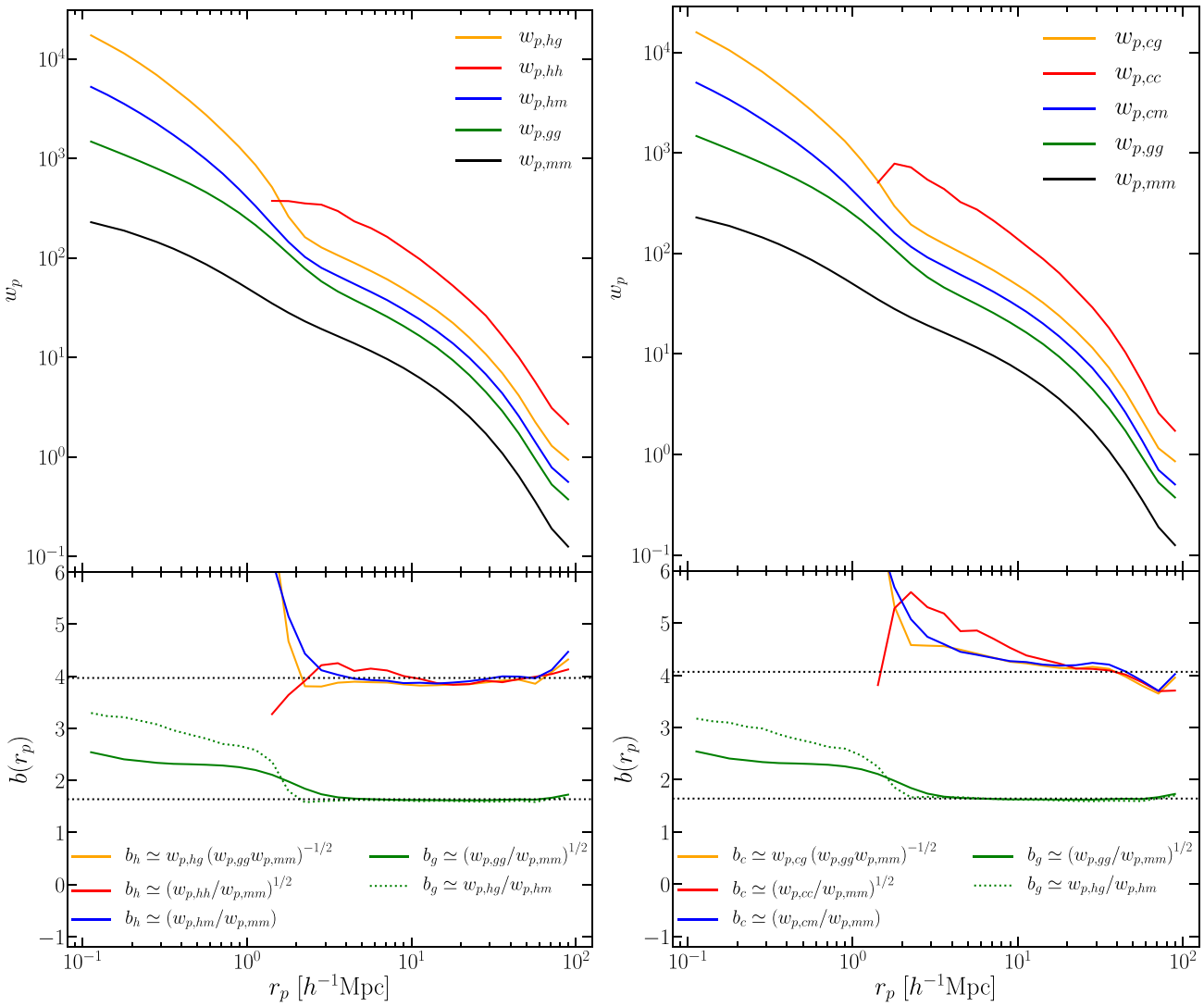

Figure 3. Analogous to Fig. 2 but for projected correlation functions $w_{\rm p}(r_{\rm p})$. Left: haloes. The average halo bias $b_{\rm h}$ and galaxy bias $b_{\rm g}$ at scales larger than $10\,h^{-1}$ Mpc are 3.97 and 1.64, respectively, shown as the horizontal dotted lines. Right: clusters. The average cluster bias $b_{\rm c}$ and $b_{\rm g}$ at scales larger than $10\,h^{-1}$ Mpc are 4.07 and 1.73, respectively.

function via

$$w_{\rm p,AB}(r_{\rm p}) = 2 \int_0^{\Pi_{\rm max}} \xi_{\rm AB}(r_{\rm p}, \pi){\rm d}\pi, \tag{7}$$

where π is the line-of-sight distance, $\Pi_{\rm max}$ is the integration limit along the line of sight, and $r_{\rm p}$ is the projected distance perpendicular to the line of sight.

Parallel to ξ, we compute the following projected correlation functions: galaxy–galaxy $w_{\rm p,gg}$, cluster–galaxy $w_{\rm p,cg}$, and cluster–matter $w_{\rm p,cm}$. We note that $w_{\rm p,cm}$ is related to cluster weak lensing signal $\Delta\Sigma$ via a linear transformation (see e.g. Park, Rozo & Krause 2021).

We use CORRFUNC to compute $\xi_{\rm gg}(r_{\rm p}, \pi)$, $\xi_{\rm cg}(r_{\rm p}, \pi)$, and $\xi_{\rm cm}(r_{\rm p}, \pi)$ in 30 logarithmically spaced bins with $0.1 < r_{\rm p} < 100\,h^{-1}$ Mpc, and in linearly spaced π bins with $\Delta\pi = 1\,h^{-1}$ Mpc out to $\Pi_{\rm max} = 100\,h^{-1}$ Mpc. We then sum over the π bins to obtain $w_{\rm p}(r_{\rm p})$. Fig. 3 shows our measurements of various $w_{\rm p}(r_{\rm p})$ functions averaged over 20 mock catalogues.

In this work, we use the true 3D positions of galaxies and clusters and do not simulate the photometric redshift uncertainties. For DES, the redshift uncertainties of redMaPPer clusters are $\sigma_z/(1+z) \approx 0.01$ (Rykoff et al. 2016), and those of redMaGiC galaxies are $\sigma_z/(1+z) \approx 0.017$ (Rozo et al. 2016). The former is likely to be negligible, while the latter can be approximated by a Gaussian distribution. In general, the impact of photometric redshift errors is to suppress two-point correlation functions consistently across all scales. For a detailed treatment for photometric redshift uncertainties, we refer readers to Wang et al. (2019).

3.2 Self-calibrated selection bias

We start by examining the self-consistency between the 3D correlation functions $\xi(r)$ between clusters, galaxies, and matter. We then use the 2D projected correlation functions $w_{\rm p}(r_{\rm p})$ to self-calibrate selection bias at scales greater than $10\,h^{-1}$ Mpc.

The left-hand panel of Fig. 2 shows the 3D correlation functions for haloes above the $2 \times 10^{14}\ h^{-1}\,{\rm M}_\odot$ threshold, and the right-

Table 3. Summary of the halo and cluster bias values derived from ξ and w_p, and the mean halo mass, averaging over 20 realizations of the mock catalogues. The cluster sample has a lower mean mass but a higher bias, indicating the impact of selection bias.

Property	Haloes	Clusters
3D bias from ξ	3.89	4.06
2D bias from w_p	3.97	4.07
Mean mass ($10^{14}\ h^{-1}\ M_\odot$)	3.28	2.99

hand panel shows the analogous calculations for richness-selected clusters with the same number density. We measure the correlation functions between 0.1 and 100 h^{-1} Mpc and average over the 20 phases in ABACUS COSMOS. The halo autocorrelation curve starts from 2 h^{-1} Mpc because of the halo exclusion effects on small scales.

In the lower panel, we show the halo bias b_h and galaxy bias b_g using various combinations of correlation functions. The green solid and dotted curves correspond to galaxy bias b_g computed as

$$b_g = \left(\frac{\xi_{gg}}{\xi_{mm}}\right)^{1/2}, \quad b_g = \frac{\xi_{hg}}{\xi_{hm}}, \tag{8}$$

while red, blue, and orange curves correspond to halo bias b_h computed as

$$b_h = \left(\frac{\xi_{gg}}{\xi_{mm}}\right)^{1/2}, \quad b_h = \frac{\xi_{hm}}{\xi_{mm}}, \quad b_h = \frac{\xi_{hg}}{\xi_{gg}\xi_{mm}^{\ 1/2}}. \tag{9}$$

These combinations of correlation functions are largely consistent with each other at large scales, demonstrating the validity of the linear bias model. The bias calculated using the halo autocorrelation function (red) mildly disagrees with the bias calculated using cross-correlations below $\approx 20\,h^{-1}$ Mpc due to halo exclusion.

Averaging over the solid green curves above 10 h^{-1} Mpc, we obtain $b_g \approx 1.62$. The bias is approximately scale-independent above 2 h^{-1} Mpc. Similarly, averaging over the blue and orange above 10 h^{-1} Mpc gives $b_h \approx 4$. In the right-hand panels, we apply the same procedure to cluster observables. We add horizontal dotted lines to indicate the large-scale bias values.

We apply the same procedure (mass cut, abundance matching, and CORRFUNC pair counts) to calculate the projected correlation functions $w_p(r_p)$, which are presented in Fig. 3.

From Figs 2 and 3, we obtain four halo bias and cluster bias values (also summarized in Table 3):

(i) $b_{h,3D}$: 3.89 (from ξ)
(ii) $b_{c,3D}$: 4.06 (from ξ)
(iii) $b_{h,2D}$: 3.97 (from w_p)
(iv) $b_{c,2D}$: 4.07 (from w_p)

The halo bias values inferred from ξ and w_p ($b_{h,3D}$ and $b_{h,2D}$) are consistent with each other, indicating that our calculations are self-consistent and that the linear bias model can be applied to our projected correlation functions. We also include the mean mass of our halo and cluster samples averaged over all 20 phases in Table 3. The cluster sample has a lower mean mass due to the scatter in the richness–mass relation and the steepness of the mass function.

Focusing first on the halo bias and cluster bias from ξ ($b_{h,3D}$ and $b_{c,3D}$), we observe that $b_{h,3D} < b_{c,3D}$. Given that the latter has a lower mean mass, we would expect a lower bias. However, our results show that the latter has a higher bias despite the lower mean mass. This indicates that the cluster selection bias is already present in the 3D, non-projected correlation functions. Our mock cluster catalogues are constructed by counts-in-cylinders along the line of sight, and therefore we expect a line-of-sight boost in the correlation function. The spherically averaged 3D correlation function does not eliminate this boost and still exhibits selection bias.

Turning our attention to the cluster bias values inferred from ξ and w_p ($b_{c,3D}$ and $b_{c,2D}$), we observe that they are roughly equal. Given that w_p is a projected quantity, one would expect that the line-of-sight boost impacts w_p more strongly than ξ. However, we find that the projection effects boost both similarly. This suggests that the boosted signal from projection effects is due to a correlation between 3D density and richness that propagates into measurements of 2D clustering.

In our previous work (Wu et al. 2022), we have used the Buzzard simulations to calibrate the impact of optical selection bias on $w_{p,cm}$ and ξ_{cm}. There, we have shown that both $w_{p,cm}$ (equivalent to the surface mass density Σ) and ξ_{cm} (equivalent to the 3D mass density ρ) exhibit strong selection bias at $\sim 1\ h^{-1}$ Mpc but have vanishing selection bias at large scales. In contrast, this work expands to a much larger scale and includes a much larger cluster sample, and we find a non-vanishing boost at large scales and in 3D correlation functions. We will discuss this point further in Section 5.

3.3 Consistency between correlation functions

Before fitting for the parameters, we verify that the correlation functions derived from mock data are consistent with the theoretical expectation. Fig. 4 compares the $w_{p,mm}$ calculated directly from simulation particles (solid) with $w_{p,mm}$ derived from galaxy and cluster catalogues assuming linear bias (dotted and dash–dotted). We can see that the $w_{p,mm}$ functions derived from the observables have an excess of $\lesssim 5$ per cent at scales larger than 10 h^{-1} Mpc. This excess is much smaller than the uncertainty levels of DES (see Fig. 5). Therefore, we expect that combining these three correlation functions would allow us to constrain cosmological parameters together with the bias parameters self-consistently.

4 LIKELIHOOD ANALYSIS

Having verified the accuracy of the linear bias model for projected correlation functions at scales larger than 10 h^{-1} Mpc, we perform a likelihood analysis using three w_p functions to constrain the cosmological parameters (Ω_M and σ_8) and bias parameters (b_c and b_g) simultaneously.

4.1 Data vector and covariance matrix

The observational data vector consists of the projected correlation functions $w_{p,cm}$, $w_{p,cg}$, and $w_{p,gg}$, averaged over 20 ABACUS COSMOS realizations (the right-hand panel in Fig. 3):

$$\boldsymbol{x}_{obs} = \left\{ w_{p,cm}(r_p),\ w_{p,cg}(r_p),\ w_{p,gg}(r_p) \right\}. \tag{10}$$

We use 10 logarithmic-spaced r_p bins between 10 and 100 h^{-1} Mpc.

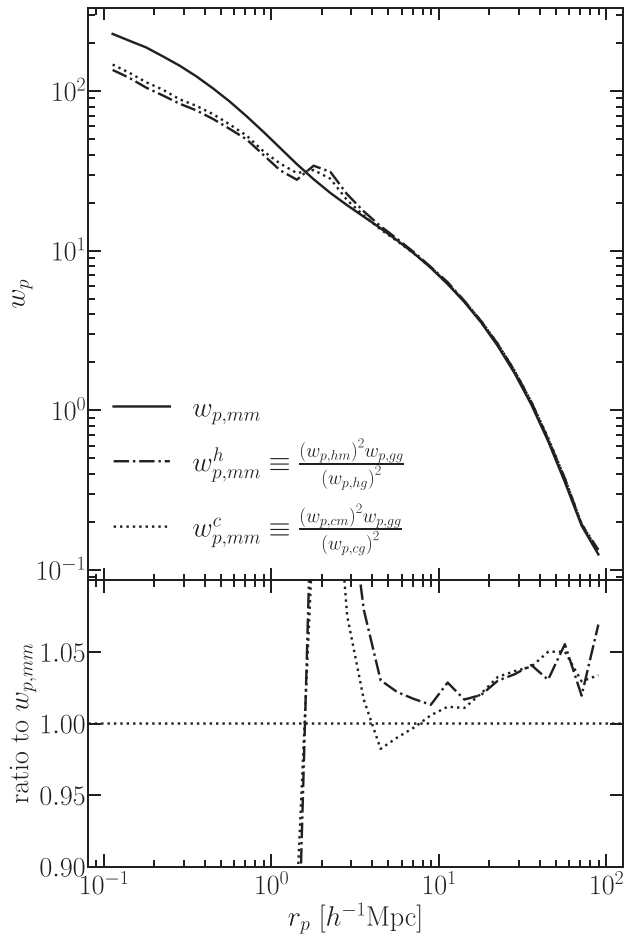

Figure 4. Projected matter autocorrelation function $w_{\rm p,mm}$ derived from the combination of halo/cluster and galaxy correlation functions. The dash–dotted curve comes from halo correlation functions, and the dotted curve comes from cluster correlation functions. The solid curve is calculated with the dark matter particles from the simulations. The bottom panel shows the ratio of the $w_{\rm p,mm}$ derived from observables with respect to the solid curve. The excess of $w_{\rm p,mm}$ derived from observables is much smaller than the uncertainty level of DES.

The corresponding model data vector is calculated with

$$\boldsymbol{x}_{\rm model} = \left\{ b_{\rm c} w_{\rm p,mm}(r_{\rm p}),\ b_{\rm g}^2 w_{\rm p,mm}(r_{\rm p}),\ b_{\rm c} b_{\rm g} w_{\rm p,mm}(r_{\rm p}) \right\} , \qquad (11)$$

where $w_{\rm p,mm}$ is calculated using the linear matter power spectrum $P(k)$ as calculated by CAMB (Lewis, Challinor & Lasenby 2000) for a given set of cosmological parameters.

To calculate the covariance matrix of $w_{\rm p,cm}$, we first calculate the covariance matrix of $\Delta\Sigma$ based on the approach presented in Wu et al. (2019). The covariance is dominated by shape noise at small scales and large-scale structure noise at large scales. We assume a DES-like survey condition: a sky coverage of 5000 deg^2, clusters at $0.2 < z_{\rm lens} < 0.35$ (corresponding to a comoving volume 0.37 h^{-3} Gpc^3) and above 2×10^{14} h^{-1} M$_\odot$, and source galaxies at $z_{\rm source} = 0.75$ with a surface density 10 arcmin^{-2}. To convert from the covariance matrix of $\Delta\Sigma$ to that of $w_{\rm p,hm}$, we apply the linear transformation presented in Park et al. (2021). We note that the $b_{\rm c}$ affects the lensing noise, and we use the bias corresponding to haloes of 2×10^{14} h^{-1} M$_\odot$ instead of the abundance-matched clusters because the former is closer to our $b_{\rm c}$ from mock catalogues.

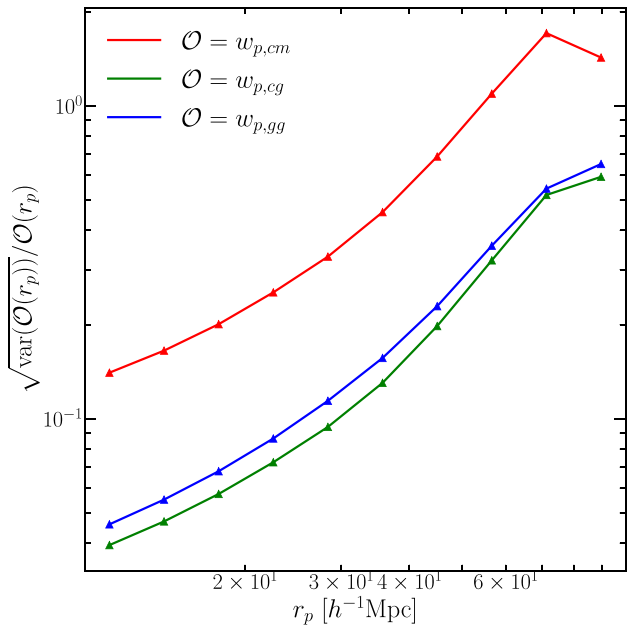

Figure 5. Fractional uncertainties for the three correlation functions, assuming a DES-like survey condition: 5000 deg^2, for clusters at $0.2 < z < 0.35$. The lensing noise is contributed by shape noise and large-scale structure noise and is the dominating uncertainty in our likelihood analysis.

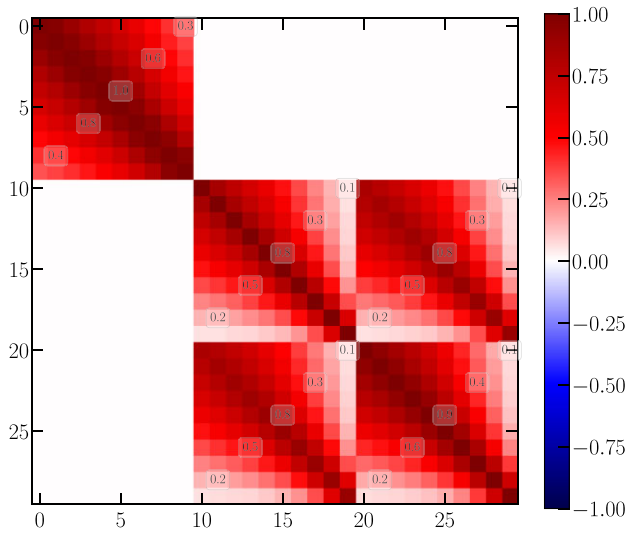

Figure 6. Correlation matrix for the three correlation functions, assuming a DES-like survey condition. Bin 0 to 9 (inclusive) refers to $w_{\rm p,cm}$, 10 to 19 refers to $w_{\rm p,cg}$, and 20 to 29 refers to $w_{\rm p,gg}$. We assume that $w_{\rm p,cm}$ is uncorrelated with $w_{\rm p,cg}$ and $w_{\rm p,gg}$ (corresponding to the white off-diagonal block) since the $w_{\rm p,cm}$ is dominated by the lensing shape noise and the foreground and background structures uncorrelated with our redshift bin.

To compute covariance matrices for $w_{\rm p,cg}$, $w_{\rm p,gg}$, and their cross-term, we use the Gaussian analytical formalism found in Salcedo et al. (2020); also see e.g. Marian, Smith & Angulo (2015) and Krause & Eifler (2017). We again assume a DES-like survey condition and use non-linear power spectra calculated from our simulations. We show the fractional error of $w_{\rm p,cm}$, $w_{\rm p,cg}$, and $w_{\rm p,gg}$ in Fig. 5 and the correlation matrix in Fig. 6. Selected diagonal values are shown in the correlation

Table 4. Parameters in our likelihood analysis. We show the fiducial values, initialization ranges, assumed priors, and best-fitting values.

Parameter	Fiducial value	Initialization	Prior range	Best-fitting value
Ω_M	0.314	[0.30, 0.32]	[0.20, 0.40]	0.310
σ_8	0.830	[0.80, 0.85]	[0.50, 1.00]	0.840
b_c	4.097	[3.80, 4.20]	[3.00, 6.00]	4.106
b_g	1.639	[1.50, 1.80]	[1.00, 3.00]	1.591

matrix.

With the ingredients above, we can calculate the χ^2 for different model vectors by

$$\chi^2 = (\boldsymbol{x}_{\rm obs} - \boldsymbol{x}_{\rm model})^T \mathbf{C}^{-1} (\boldsymbol{x}_{\rm obs} - \boldsymbol{x}_{\rm model}), \quad (12)$$

where $\mathbf{C}^{-1}$ is the inverse of the combined covariance matrix of $w_{\rm p,cm}$, $w_{\rm p,cg}$, and $w_{\rm p,gg}$. This χ^2 is used as the negative two times the log-likelihood function in the MCMC calculation.

4.2 Parameter inference

We perform a likelihood analysis to constrain Ω_M, σ_8, b_c, and b_g using the parallel affine-invariant ensemble sampler (Goodman & Weare 2010) implemented in the PYTHON module EMCEE[3] (Foreman-Mackey et al. 2013).

We initialize 200 walkers uniformly using the initialization range listed in Table 4. The initialization of walkers enables the parallelization of the code, where processors handle multiple walkers simultaneously. The small range of initialization does not limit the exploration range of the sampler because walkers quickly branch out and reach the rest of the parameter space. We assume flat priors that are listed in the 'Prior range' column of the table. The final chain has 184 000 steps in total, and we remove the first 18 000 as the burn-in. The chain was stopped according to the integrated autocorrelation time criteria. At the end of the chain, the ratio between the number of samples and the autocorrelation time is 22.

Fig. 7 shows our posterior distribution of parameters, generated using the CORNER software package (Foreman-Mackey 2016). The contours refer to 68 and 95 per cent boundaries, and the blue vertical and horizontal lines refer to fiducial parameter values. All contours capture the true values in the 68 per cent level. We compare various χ^2 values:

(i) $\chi^2_{\rm fid} = 5.583$
(ii) $\chi^2_{\rm best\text{-}fitting} = 3.380$
(iii) $\chi^2_{\rm median} = 3.421$

The degrees of freedom are 26, and thus the χ^2 per degree of freedom is much less than 1. Since the total volume of our simulations is approximately 70 times the survey volume, we expect the data vector to be much less noisy than real data, and thus the χ^2 per degree of freedom is small.

Overall, we see that Ω_M is constrained at the 4.1 per cent level and that σ_8 is constrained at the 12.4 per cent level. The modest constraint on σ_8 is due to the strong degeneracy with b_c and b_g, both constrained at the 10 per cent level. In comparison, in table 5 in Salcedo et al. (2020), the row corresponding to the large-scale (3 h^{-1} Mpc) $\Delta\Sigma$, $w_{\rm p,cg}$, and $w_{\rm p,gg}$ leads to a 3.7 per cent constraint on σ_8 with fixed Ω_M. Our constraints on σ_8 are weaker due to the larger scale cut and the free Ω_M. This comparison highlights the benefit of a stronger prior on Ω_M and smaller scale cuts.

We note that the contour of σ_8 and Ω_M does not show the usual anticorrelation from cluster number counts (e.g. Y1CL). Fig. 8 in Salcedo et al. (2020) shows that the σ_8 and Ω_M have the opposite effect in determining $w_{\rm p,gg}$ and $w_{\rm p,cg}$; that is, their derivatives with respect to σ_8 and Ω_M have opposite signs. Therefore, the constraints from the cluster and galaxy clustering signals are highly complementary to the constraints from cluster abundance and lensing.

In Fig. 8, we present the best-fitting model, together with the data vector and its uncertainties. Since the uncertainties increase with scale (also see Fig. 5), the best-fitting model is mostly driven by the smallest r_p bins. At larger scales, the $w_{\rm p,mm}$ predicted by the best-fitting parameters shows a small excess compared with the $w_{\rm p,mm}$ from mock. This is related to the small excess shown in Fig. 4 and the slightly larger Ω_M and σ_8 compared with the true values. This excess is much smaller than the current level of experimental uncertainties but would require further examination for future data sets.

5 DISCUSSIONS

In this section, we discuss our results in the context of previous studies. We will then describe our plans for further developing the model and applying our method to real data.

5.1 Comparison with previous studies

Using *N*-body simulations, Osato et al. (2018) have shown that cluster surface density profiles exhibit a strong dependence on the orientation with respect to the line of sight (also see e.g. Dietrich et al. 2014; Zhang et al. 2023). They have shown that this orientation dependence extends to 100 h^{-1} Mpc and can be explained by the anisotropic halo–matter correlation function $\xi_{\rm hm}(s, \mu)$. For a mass-selected halo sample, we expect that averaging over all haloes and all μ would recover the isotropic $\xi_{\rm hm}(r)$. The fact that we find $\xi_{\rm cm}$ higher than $\xi_{\rm hm}$ indicates that the richness selection prefers clusters with more strongly anisotropic $\xi_{\rm hm}$ (e.g. due to the filaments along the line of sight). Our finding is consistent with their results of non-vanishing large-scale selection bias due to projection.

Using mock cluster catalogues constructed from an HOD model, Sunayama et al. (2020) have demonstrated that the cluster lensing and cluster clustering signal are boosted relative to an isotropic halo model. Such a boost persists to large scales. Their fig. 13 shows that clusters that suffer from strong projection effects exhibit a highly anisotropic projected correlation function, indicating the existence of line-of-sight filaments.

In our previous work (Wu et al. 2022), we have studied the cluster projection effects using the mock redMaPPer catalogues constructed from the Buzzard simulations, which are designed for DES mock analysis. We have used the full dark matter particles from the simulations and have focused on relatively small scales ($<3\,h^{-1}$ Mpc for $\xi_{\rm hm}$ and $<30\,h^{-1}$ Mpc for $w_{\rm p,cm}$). Those results have hinted at a vanishing selection bias for both $\xi_{\rm hm}$ and $w_{\rm p,cm}$ at large scales. In addition, the Buzzard simulations have a lower cluster abundance compared with observed clusters.

In this paper, we focus on a regime complementary to Wu et al. (2022). We construct mock catalogues with a simple yet realistic HOD that matches DES cluster abundance, use large-volume *N*-body simulations, and focus on large-scale correlation functions.

[3]We use EMCEE 3.1.1, CORRFUNC 2.4.0, CAMB 1.3.2, and CORNER 2.2.1 in our calculations.

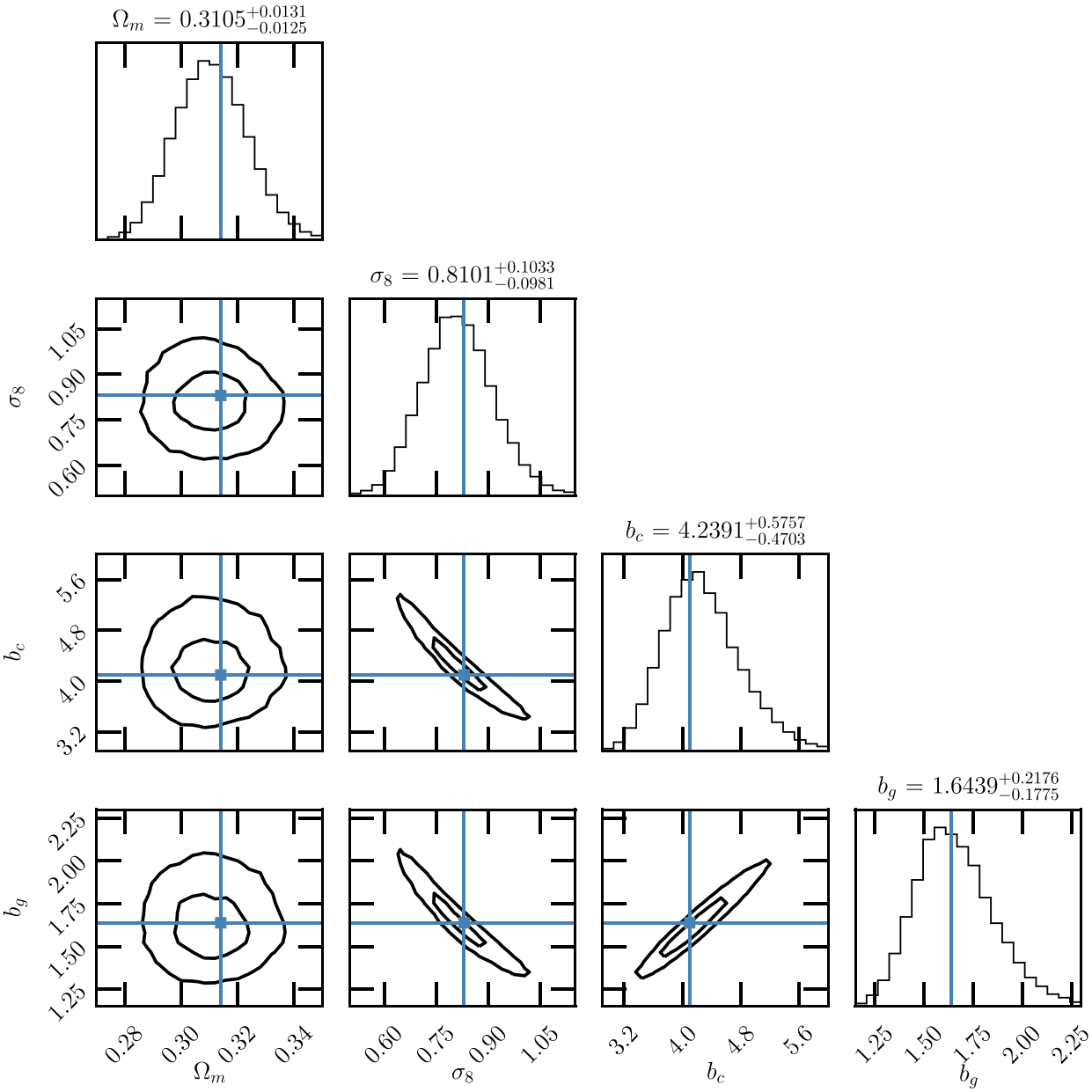

Figure 7. Posterior distribution of cosmological parameters ($\Omega_{\rm M}$ and σ_8) and nuisance parameters (cluster bias $b_{\rm c}$ and galaxy bias $b_{\rm g}$), derived from fitting projected cross-correlation functions $w_{\rm p,cm}$, $w_{\rm p,cg}$, and $w_{\rm p,gg}$. The contours correspond to 68 and 95 per cent levels. The blue lines refer to true parameter values. All contours capture the true values in the 68 per cent level. The calculated χ^2 per degree of freedom is small ($\approx$0.2) because the total volume of our simulations is approximately 70 times the survey volume, and the data vector is much less noisy than real data.

We have found that the large-scale selection bias is non-vanishing and approaches a constant for $\xi_{\rm cm}$ and $w_{\rm p,cm}$. In particular, the $\xi_{\rm cm}$ selection bias is associated with projection effects, which is confirmed by calculating $\xi_{\rm cm}$ in various orientations.

The measurements of cluster clustering have recently come to fruition due to the availability of large-area survey data (e.g. Chiu et al. 2020; To et al. 2021; Park et al. 2023). These analyses have considered or incorporated cluster selection bias in various ways. Chiu et al. (2020) use the autocorrelation and cross-correlation functions ($\xi_{\rm cc}$, $\xi_{\rm cg}$, and $\xi_{\rm gg}$) between Hyper Suprime-Cam's CAMIRA (Cluster finding algorithm based on Multi-band Identification of Red sequence gAlaxies) cluster catalogue and the CMASS (ConstantMASS)) galaxy catalogue to constrain the normalization of the richness–mass relation. They have assessed the impact of selection bias and concluded that it is unimportant for their data set but would be necessary for future studies. To et al. (2021) combine redMaPPer cluster abundance with the autocorrelation and cross-correlation functions between clusters, galaxies, and weak lensing shear. They focus on the angular correlation function $w(\theta)$ and find that the selection bias is at the 15 per cent level at scales greater than 8 h^{-1} Mpc. Park et al. (2023) use cluster abundance, cluster lensing, and cluster clustering of the SDSS (the Sloan Digital Sky Survey) redMaPPer catalogue and apply an empirical model for the projection effect. They have found a 15–20 per cent anisotropic boost, similar to that in To et al. (2021). They have found a lower $\Omega_{\rm M}$ and higher σ_8 compared with the *Planck* results.

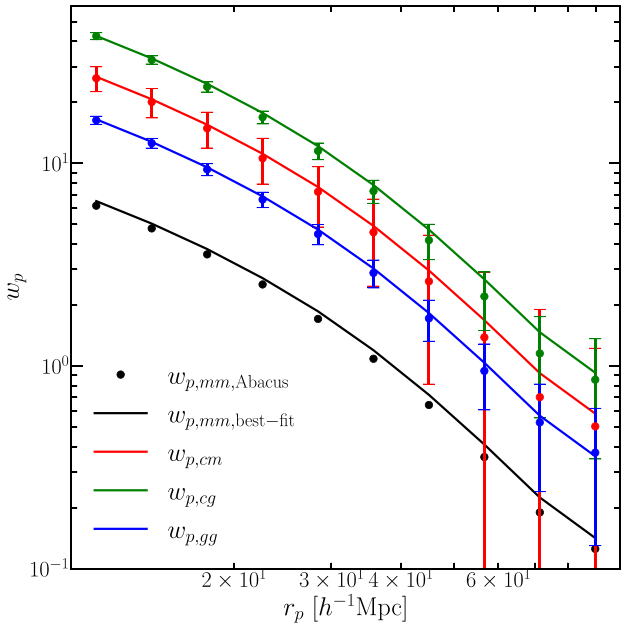

Figure 8. The best-fitting model (colour curves) compared with the input data vector from our mock catalogues (colour points with error bars). The black curve shows the analytical $w_{\mathrm{p,mm}}$ from the best-fitting parameters, and the black points show the $w_{\mathrm{p,mm}}$ from mocks.

Our results imply that the projection effects impact not only the projected correlation functions but also the 3D correlation function. In both cases, we can self-consistently model the large-scale cross-correlation functions between clusters, galaxies, and shear and use them to solve for the selection bias. We have not considered constraints from small-scale correlation functions, which are more difficult to model but have enormous constraining power (Salcedo et al. 2020, 2022). Modelling the small-scale correlation function would require extra nuisance parameters, which may weaken the constraining power. We expect that the large-scale self-calibration we present in this work would be highly complementary to the small-scale bias calibration.

5.2 Future work

In this work, we focus on cluster selection bias and simplify the assumptions on other systematic uncertainties. In particular, we use the 3D positions of galaxies in simulations and ignore galaxy velocities and redshift uncertainties. The redshift uncertainties of clusters are likely to remain negligible, but the photometric redshift uncertainties of galaxies need to be modelled. A full analysis would need to take into account the photometric redshift uncertainties (e.g. Wang et al. 2019) and the redshift-space distortion (e.g. Kaiser 1987; Hamilton 1998; Sunayama 2023).

We assume that the galaxy sample and the cluster sample are constructed from galaxies with different colour selection criteria, and therefore we need two separate HOD models. The different colour selection criteria are due to the fact that the galaxy sample and the cluster sample are optimized differently: the galaxy sample is optimized for a small redshift uncertainty, while the cluster sample is optimized for a small richness–mass scatter (Rykoff et al. 2014; Rozo et al. 2016). However, the different colour selection criteria lead to a large number of nuisance parameters, which could be difficult to constrain. We plan to explore the possibility of using the same colour selection criterion for both samples, which will require only one set of HOD parameters. This approach would potentially optimize both samples simultaneously and improve their constraining power on HOD parameters.

With the upcoming spectroscopic galaxy sample from the Dark Energy Spectroscopic Instrument and *Nancy G. Roman Space Telescope*, it is possible to cross-correlate cluster samples with spectroscopic galaxies (analogous to Gaztañaga et al. 2012). We expect that the spectroscopic galaxy sample would have a smaller sample size but a better-constrained HOD.

With the newly available large-area multiwavelength cluster samples, it is also possible to cross-correlate optical galaxies with clusters selected by X-ray or the SZ effect. For example, Shin et al. (2021) measure cluster lensing and galaxy clustering around clusters selected by SZ signal from the Atacama Cosmology Telescope. Compared with optical cluster samples, X-ray and SZ cluster samples focus on more massive haloes and have smaller sample sizes. Another approach would be using clusters with various mass proxies and performing both self- and cross-calibrations of cluster selection bias (see e.g. Costanzi et al. 2021).

In this work, we use the large-scale correlation function to demonstrate the feasibility of self-calibrating selection bias. On the other hand, small-scale correlation functions have enormous constraining power [see Salcedo et al. (2020, 2022) for detailed discussion]. The modelling of small-scale correlation functions would require detailed simulations covering a wide range of parameters. These simulations are usually computationally extensive, but the recent development of emulators provides an effective approach for constructing small-scale models (see e.g. Nishimichi et al. 2019; Wibking et al. 2020). We plan to apply an emulator approach to accurately model the small-scale correlation functions and their dependence on galaxy–halo connection models.

Galaxy clustering measurements suffer from various systematic uncertainties (see e.g. Weaverdyck & Huterer 2021, and references therein). For example, Pandey et al. (2022) analyse DES Y3 redMaGiC galaxy clustering and galaxy–galaxy lensing and find that the galaxy bias derived from galaxy clustering is systematically higher than the galaxy bias derived from galaxy–galaxy lensing. They parametrize this discrepancy by a decorrelation parameter X_{lens} and find that such a decorrelation can be alleviated by broadening the colour selection of the galaxy sample. This result indicates colour-dependent systematic uncertainties in the galaxy catalogue, which need to be taken into account in cluster–galaxy cross-correlation studies.

Future photometric surveys like LSST demand more stringent control of systematic uncertainties compared with DES-like surveys (see e.g. Mandelbaum 2018, for a review). For example, the blending of galaxies would become more significant, impacting the galaxy shape and photometric redshift measurements. These systematic uncertainties are likely to be resolved by the cross-calibration between LSST, Roman, and Euclid, as well as spectroscopic follow-up observations from the ground (e.g. Rhodes et al. 2017; Eifler et al. 2021).

6 SUMMARY

Using mock catalogues of galaxies and galaxy clusters based on *N*-body simulations and HOD models, we assess the efficacy of using cluster lensing, cluster–galaxy cross-correlation functions, and galaxy autocorrelation functions to self-calibrate the optical cluster selection bias. Although cluster selection bias is mostly due to projection effects, we have found that the selection bias is present

even in 3D correlation functions and extends to $\approx 100\,h^{-1}$ Mpc. Using the 2D correlation functions, $w_{\rm p,cm}$, $w_{\rm p,cg}$, and $w_{\rm p,gg}$, we show that the selection bias can be calibrated self-consistently at scales larger than $10\,h^{-1}$ Mpc (Fig. 3). We perform a likelihood analysis using a data vector derived from simulations and analytical covariance matrices assuming a DES-like survey condition (5000 deg^2, 10 source galaxies per arcmin^2, and focusing on the lowest redshift bin $0.2 < z < 0.35$ and large scale 10–100 h^{-1} Mpc). We find that $\Omega_{\rm M}$ and σ_8 are constrained at the 4.1 and 12.4 per cent levels, respectively, and exhibit only mild degeneracy. The cluster bias $b_{\rm c}$ and galaxy bias $b_{\rm g}$ are strongly degenerate with each other and are constrained at 10 per cent.

The constraints forecasted here are modest due to the conservative scale cuts we use. We have discussed strategies for pushing the modelling to small scales and applying the method to real data. Optical cluster cosmology is at a crossroads because of the newly uncovered systematic biases. The success of future cluster experiments would likely require a concerted effort of self- and cross-calibrations of cluster selection bias.

ACKNOWLEDGEMENTS

We thank Lehman Garrison and the ABACUS team for providing ABACUS COSMOS simulation suite. We thank Tomomi Sunayama, Chun-Hao To, and the anonymous reviewer for their helpful suggestions. During the preparation of this work, CZ and CMH were supported by David & Lucile Packard Foundation award 2021-72096, the Simons Foundation award 60052667, and the NASA award 15-WFIRST15-0008. H-YW was supported by the DOE award DE-SC0021916 and the NASA award 15-WFIRST15-0008. ANS was supported by the DOE awards DE-SC0009913 and DE-SC0020247.

The computations in this paper were performed on the CCAPP condo of the Pitzer Cluster at the Ohio Supercomputer Center (1987). We thank the developers for the following software packages: CAMB, EMCEE (Foreman-Mackey et al. 2013), CORNER (Foreman-Mackey 2016), and CORRFUNC (Sinha & Garrison 2017).

DATA AVAILABILITY

The data underlying this analysis will be shared upon reasonable request to the corresponding author.

REFERENCES

Abbott T. M. C. et al., 2018, Phys. Rev. D, 98, 043526
Abbott T. M. C. et al., 2020, Phys. Rev. D, 102, 023509 (Y1CL)
Allen S. W., Evrard A. E., Mantz A. B., 2011, ARA&A, 49, 409
Balaguera-Antolínez A., Sánchez A. G., Böhringer H., Collins C., Guzzo L., Phleps S., 2011, MNRAS, 413, 386
Baxter E. J., Rozo E., Jain B., Rykoff E., Wechsler R. H., 2016, MNRAS, 463, 205
Behroozi P. S., Wechsler R. H., Wu H.-Y., 2013, ApJ, 762, 109
Berlind A. A., Weinberg D. H., 2002, ApJ, 575, 587
Bleem L. E. et al., 2020, ApJS, 247, 25
Bocquet S. et al., 2015, ApJ, 799, 214
Bocquet S. et al., 2019, ApJ, 878, 55
Chiu I. N., Okumura T., Oguri M., Agrawal A., Umetsu K., Lin Y.-T., 2020, MNRAS, 498, 2030
Collins C. A. et al., 2000, MNRAS, 319, 939
Cooray A., Sheth R., 2002, Phys. Rep., 372, 1
Correa C. A., Wyithe J. S. B., Schaye J., Duffy A. R., 2015, MNRAS, 452, 1217
Costanzi M. et al., 2019, MNRAS, 482, 490
Costanzi M. et al., 2021, Phys. Rev. D, 103, 043522
Croft R. A. C., Dalton G. B., Efstathiou G., 1999, MNRAS, 305, 547
de Haan T. et al., 2016, ApJ, 832, 95
DeRose J. et al., 2019, preprint (arXiv:1901.02401)
Dietrich J. P. et al., 2014, MNRAS, 443, 1713
Dietrich J. P. et al., 2019, MNRAS, 483, 2871
Eifler T. et al., 2021, MNRAS, 507, 1514
Estrada J., Sefusatti E., Frieman J. A., 2009, ApJ, 692, 265
Foreman-Mackey D., 2016, J. Open Source Softw., 1, 24
Foreman-Mackey D., Hogg D. W., Lang D., Goodman J., 2013, PASP, 125, 306
Frieman J. A., Turner M. S., Huterer D., 2008, ARA&A, 46, 385
Garrison L. H., Eisenstein D. J., Ferrer D., Tinker J. L., Pinto P. A., Weinberg D. H., 2018, ApJS, 236, 43
Gaztañaga E., Eriksen M., Crocce M., Castander F. J., Fosalba P., Marti P., Miquel R., Cabré A., 2012, MNRAS, 422, 2904
Giles P. A. et al., 2022, MNRAS, 516, 3878
Goodman J., Weare J., 2010, Commun. Appl. Math. Comput. Sci., 5, 65
Hamilton A. J. S., 1998, in Hamilton D., ed., Astrophysics and Space Science Library, Vol. 231, The Evolving Universe. Kluwer, Dordrecht, p. 185
Huterer D. et al., 2015, Astropart. Phys., 63, 23
Kaiser N., 1987, MNRAS, 227, 1
Kovacs E. et al., 2022, Open J. Astrophys., 5, 1
Krause E., Eifler T., 2017, MNRAS, 470, 2100
Lewis A., Challinor A., Lasenby A., 2000, ApJ, 538, 473
Lima M., Hu W., 2004, Phys. Rev. D, 70, 043504
Lima M., Hu W., 2005, Phys. Rev. D, 72, 043006
Majumdar S., Mohr J. J., 2004, ApJ, 613, 41
Mana A., Giannantonio T., Weller J., Hoyle B., Hütsi G., Sartoris B., 2013, MNRAS, 434, 684
Mandelbaum R., 2018, ARA&A, 56, 393
Mantz A., Allen S. W., Rapetti D., Ebeling H., 2010, MNRAS, 406, 1759
Mantz A. B., Allen S. W., Morris R. G., Rapetti D. A., Applegate D. E., Kelly P. L., von der Linden A., Schmidt R. W., 2014, MNRAS, 440, 2077
Marian L., Smith R. E., Angulo R. E., 2015, MNRAS, 451, 1418
McClintock T. et al., 2019, MNRAS, 482, 1352
Melchior P. et al., 2017, MNRAS, 469, 4899
Metchnik M. V. L., 2009, PhD thesis, The University of Arizona
Murata R., Nishimichi T., Takada M., Miyatake H., Shirasaki M., More S., Takahashi R., Osato K., 2018, ApJ, 854, 120
Murata R. et al., 2019, PASJ, 71, 107
Navarro J. F., Frenk C. S., White S. D. M., 1997, ApJ, 490, 493
Nishimichi T. et al., 2019, ApJ, 884, 29
Ohio Supercomputer Center, 1987, Ohio Supercomputer Center, available at http://osc.edu/ark:/19495/f5s1ph73
Osato K., Nishimichi T., Oguri M., Takada M., Okumura T., 2018, MNRAS, 477, 2141
Paech K., Hamaus N., Hoyle B., Costanzi M., Giannantonio T., Hagstotz S., Sauerwein G., Weller J., 2017, MNRAS, 470, 2566
Pandey S. et al., 2022, Phys. Rev. D, 106, 043520
Park Y., Rozo E., Krause E., 2021, Phys. Rev. Lett., 126, 021301
Park Y., Sunayama T., Takada M., Kobayashi Y., Miyatake H., More S., Nishimichi T., Sugiyama S., 2023, MNRAS, 518, 5171
Peebles P. J. E., 1980, The Large-Scale Structure of the Universe. Princeton Univ. Press, Princeton, NJ
Planck Collaboration XIII , 2016, A&A, 594, A13
Press W. H., Schechter P., 1974, ApJ, 187, 425
Rhodes J. et al., 2017, ApJS, 233, 21
Rozo E., Rykoff E. S., 2014, ApJ, 783, 80
Rozo E. et al., 2010, ApJ, 708, 645
Rozo E., Rykoff E. S., Becker M., Reddick R. M., Wechsler R. H., 2015, MNRAS, 453, 38
Rozo E. et al., 2016, MNRAS, 461, 1431
Rykoff E. S. et al., 2014, ApJ, 785, 104
Rykoff E. S. et al., 2016, ApJS, 224, 1
Salcedo A. N., Wibking B. D., Weinberg D. H., Wu H.-Y., Ferrer D., Eisenstein D., Pinto P., 2020, MNRAS, 491, 3061

Salcedo A. N., Weinberg D. H., Wu H.-Y., Wibking B. D., 2022, MNRAS, 510, 5376
Sánchez A. G., Lambas D. G., Böhringer H., Schuecker P., 2005, MNRAS, 362, 1225
Saro A. et al., 2015, MNRAS, 454, 2305
Schuecker P., Böhringer H., Collins C. A., Guzzo L., 2003, A&A, 398, 867
Sheth R. K., Mo H. J., Tormen G., 2001, MNRAS, 323, 1
Shin T. et al., 2021, MNRAS, 507, 5758
Simet M., McClintock T., Mandelbaum R., Rozo E., Rykoff E., Sheldon E., Wechsler R. H., 2017, MNRAS, 466, 3103
Sinha M., Garrison L., 2017, Astrophysics Source Code Library, record ascl:1703.003
Sunayama T., 2023, MNRAS, 521, 5064
Sunayama T. et al., 2020, MNRAS, 496, 4468
Tinker J. L., Kravtsov A. V., Klypin A., Abazajian K., Warren M., Yepes G., Gottlöber S., Holz D. E., 2008, ApJ, 688, 709
To C. H. et al., 2021, Phys. Rev. Lett., 126, 141301
Vikhlinin A. et al., 2009, ApJ, 692, 1060
Wang Z. et al., 2019, ApJ, 879, 71
Weaverdyck N., Huterer D., 2021, MNRAS, 503, 5061
Weinberg D. H., Mortonson M. J., Eisenstein D. J., Hirata C., Riess A. G., Rozo E., 2013, Phys. Rep., 530, 87
Wibking B. D., Weinberg D. H., Salcedo A. N., Wu H.-Y., Singh S., Rodríguez-Torres S., Garrison L. H., Eisenstein D. J., 2020, MNRAS, 492, 2872
Wu H.-Y., Rozo E., Wechsler R. H., 2008, ApJ, 688, 729
Wu H.-Y., Weinberg D. H., Salcedo A. N., Wibking B. D., Zu Y., 2019, MNRAS, 490, 2606
Wu H.-Y., Weinberg D. H., Salcedo A. N., Wibking B. D., 2021, ApJ, 910, 28
Wu H.-Y. et al., 2022, MNRAS, 515, 4471
Zehavi I. et al., 2011, ApJ, 736, 59
Zhang Z. et al., 2023, MNRAS, 523, 1994
Zheng Z. et al., 2005, ApJ, 633, 791

This paper has been typeset from a TEX/LATEX file prepared by the author.